Electron beam size monitoring at the SLS 2.0 using Fresnel zone plates

C. Ozkan Loch, M. Aiba, and X. Wang
Center for Accelerator Science and Engineering, Paul Scherrer Institute, CH-5232 Villigen PSI, Switzerland

J. Vila-Comamala
Center for Photon Science, Paul Scherrer Institute, CH-5232 Villigen PSI, Switzerland

(Received 14 April 2026; accepted 23 October 2026; published 17 November 2026)

The Swiss Light Source (SLS) storage ring has been rebuilt as SLS 2.0, providing an electron beam with significantly reduced horizontal emittance. This upgrade enables an x-ray beam with brightness increased by nearly 2 orders of magnitude and extends the accessible photon-energy range by approximately 50%. Precise characterization of the electron source is crucial for optimizing and fully exploiting the performance of new fourth-generation light sources. However, conventional methods for determining the electron beam source size, such as pinhole-based imaging, lack the resolution needed to characterize sub −10 μm beam sizes, thus motivating the development of advanced diagnostic approaches. Here, we employ a Fresnel zone plate-based system to measure the electron source size at the SLS 2.0 storage ring. We demonstrate the measurement of sub−10 μm electron beam sizes and discuss challenges and potential future improvements of the proposed monitor.

DOI: 10.1103/jjb6-4fr1

I. INTRODUCTION

Electron-beam transverse size is a fundamental parameter determining photon-beam brightness, coherence, and spectral performance in synchrotron light sources. Fourth-generation light sources are designed to achieve a natural horizontal emittance on the order of a few hundred picometers, or even below 100 pm rad. The vertical emittance is typically tuned according to operational requirements, ranging from approximately 10 pm rad to about half of the natural horizontal emittance. Since these emittance values correspond to beam sizes in the micrometer regime, reliable diagnostics for transverse electron beam profile measurements are essential for storage-ring commissioning, transverse coupling control, and routine operation monitoring.

Resolving such small beam dimensions is, however, challenging, as conventional visible-light imaging is fundamentally limited by diffraction and optical aberrations. A range of radiation-based diagnostic techniques has been explored and implemented at various facilities, including pinhole imaging [1] and interferometric methods—such as double-slit and grating interferometry—which infer beam size through spatial coherence [2]. The former, although conceptually simple, is intrinsically limited in resolution. Having a pinhole with the right dimensions (<10 μm) is technologically very challenging and would mean a trade-off between photon flux and spatial resolution. The latter requires precise alignment and sufficiently high photon intensity, while also imposing stringent demands on mechanical and optical stability.

In a recent systematic study, Samadi *et al*. compared several electron source-size measurement techniques—including pinhole imaging, interferometry, and a K-edge filter phase-space beam position and size monitor—under comparable operating conditions at a low-emittance storage ring [3]. The results highlighted the respective strengths and limitations of each method for low-emittance machines and underscored the need for diagnostic approaches capable of direct imaging with both high-spatial resolution and robust operational performance.

Given the small beam sizes to be measured, x-ray synchrotron radiation (SR) provides a means to overcome classical diffraction limits by exploiting short-wavelength optics. Fresnel zone plates (FZPs), which are diffractive x-ray lenses, can achieve submicrometer spatial resolution within relatively compact optical configurations. Their resolving power is primarily determined by the outermost zone width, allowing enhanced spatial resolution without incurring prohibitive photon-flux loss. Compared with interferometric techniques, FZP-based systems offer direct imaging of the source distribution, making them highly attractive candidates for continuous transverse beam size diagnostics.

Published by the American Physical Society under the terms of the Creative Commons Attribution 4.0 International license. Further distribution of this work must maintain attribution to the author(s) and the published article's title, journal citation, and DOI.

FZPs for beam diagnostics were first implemented at the KEK Accelerator Test Facility, where synchrotron radiation from a bending magnet was monochromatized and magnified using a two-FZP system, achieving submicrometer spatial resolution. This approach enabled precise measurements of electron beam sizes, damping times, and coupling, providing a high-resolution and reliable diagnostic platform critical for the development of linear-collider-ready ultralow-emittance beams [4,5]. FZPs have also been employed at the SPring-8 storage ring to observe transverse beam profiles for emittance measurements. Using FZPs, they successfully characterized electron beam profiles and resolved a vertical emittance below 10 pm rad at a circulating current of 10 mA [6]. In addition, FZPs have been tested at the Swiss Light Source (SLS) for beam profile measurements [7].

The first implementation of FZP-based transverse beam size measurement in the context of a fourth-generation light source has recently been realized at the Swiss Light Source upgrade, SLS 2.0. During the initial commissioning phase, continuous two-dimensional x-ray beam size measurements using FZPs were successfully demonstrated, with vertical and horizontal beam sizes on the order of 10 μm at typical operating currents, confirming the feasibility of this approach. Previous studies at the legacy SLS facility also investigated x-ray FZP imaging, yielding promising results for simultaneous two-dimensional profile measurements and providing a foundation for the SLS 2.0 implementation.

Despite these advances, FZP-based diagnostics have not yet been widely adopted or systematically evaluated in the demanding environment of the fourth-generation light-source storage rings, where submicrometer resolution, as well as mechanical and thermal stability, are critical. Key challenges include optimizing photon flux and signal-to-noise ratio (S/N) for rapid measurements and balancing spatial resolution with magnification in the optical design.

In this work, we present the design, implementation, performance characterization, and operational results of a transverse beam size diagnostic based on a Fresnel zone plate, implemented at SLS 2.0. We demonstrate its capability to resolve ultrasmall beam features under realistic operating conditions and examine both challenges and future improvements as a tool for routine beam monitoring in low-emittance storage rings.

II. BEAM SIZE MONITOR DESIGN

SLS 2.0 is a fourth-generation light source based on a multibend achromat lattice with a substantially reduced transverse electron beam emittance and increased brightness and transverse coherence of the generated x-ray radiation. The upgraded storage ring operates at an electron energy of 2.7 GeV with a stored beam current of 400 mA in top-up mode, reusing the tunnel infrastructure from the original SLS accelerator [8]. The relevant parameters are listed in Table I.

The SLS 2.0 lattice achieves a natural horizontal emittance in a range of 130–160 pm rad (depending on the setting of the photon sources in the machine), representing a reduction of more than an order of magnitude compared to the original SLS storage ring. The vertical emittance is regulated by manipulating transverse coupling to be approximately 10 pm rad [9], corresponding to an emittance ratio of several percent.

The transverse electron beam sizes at the radiation source points are determined by the local beta and dispersion functions and the corresponding emittances and energy spread. For bending magnets, the resulting root-mean-square (rms) electron beam sizes have representative values of approximately 8–9 μm horizontally and 6–8 μm vertically, depending on the specific optics configuration. These small source sizes, combined with correspondingly low angular divergences, enable a substantial increase in spectral brightness and coherent photon flux across a wide photon-energy range.

For commissioning and standard machine operation, the range of interest of the vertical beam size to be measured is 2–28 μm and 5–12 μm for the horizontal beam size. The resolution needed to measure an emittance change of 1 pm rad vertically is 0.4 μm.

FZPs have been employed to enable direct, high-resolution imaging of the source size and to allow precise characterization of sub−10 μm electron beams and their

TABLE I. Parameters of the SLS 2.0 storage ring [8].

Parameters	Values	Remark
Storage ring circumference	288 m	Existing ring tunnel
Electron energy	2.7 GeV	Increased from 2.4 GeV
Stored current (top-up)	400 mA	Same as before upgrade
Natural (horizontal) emittance	131–158 pm rad	Variation primarily due to IDs
Vertical emittance	10 pm rad	Nominal coupling-controlled value
Electron beam size (rms)	8–9 μm (H and V)	Expected at monitor source point; varies with optics
Coherence fraction	0.066	At 10 keV for a natural emittance of 150 pm rad

relative changes in both transverse directions. Building on our previous experiments at the legacy SLS storage ring [7], both single- and double-FZP imaging configurations were explored: a single FZP provides faster source-size measurements, but high-resolution imaging requires a long system length. The addition of a second magnifying FZP relaxes the total length requirement of the system, while still achieving high-resolution imaging of the source. In both configurations, the FZPs are used in transmission geometry, which is straightforward to align and delivers sufficient flux for imaging with short camera exposure times.

A. Layout

The beam size monitor was designed based on two limitations: the system had to be confined within the space of the accelerator tunnel (approximately 12 m), and the first FZP could not be situated closer than 7 m to the source. Due to these limitations, a single FZP only allows the realization of a demagnifying geometry, which is not ideal because it would require a detector to resolve an image source of 1–2 μm. For this reason, a second zone plate was introduced to magnify the image onto the detector. The first FZP is, hereafter, referred to as an objective zone plate (OZP), and the second FZP is referred to as a magnifying zone plate (MZP). The MZP used with the OZP in tandem resembles a full-field transmission x-ray microscope (TXM). From here on, this combination will be referred to as the TXM setup.

Figure 1(a) shows the concept of the beam size monitor using only the OZP; Fig. 1(b) shows the setup using both OZP and MZP. Figure 1(c) shows the 3D model of the

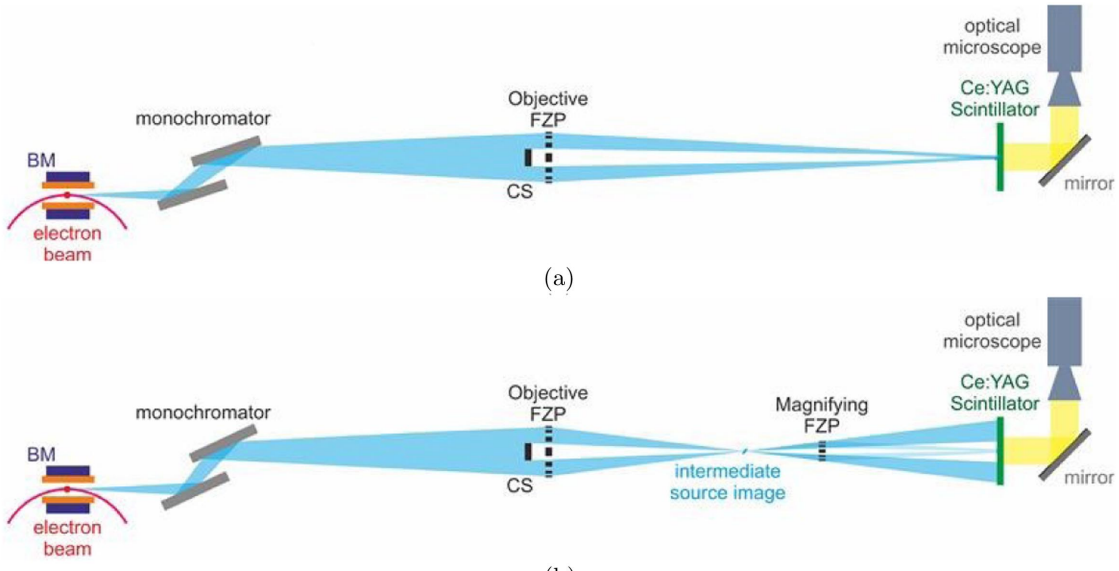


FIG. 1. Conceptual sketch of the FZP-based electron beam size monitor at the SLS 2.0 using (a) only the OZP setup or (b) the TXM setup. (c) 3D model of the monitor at SLS 2.0. To change from the OZP to the TXM setup, the monochromator Bragg angle is changed to focus the beam on the imaging system. The Bragg angle corresponds to 20 keV for the OZP and 11.8 keV for the TXM setup.

system constructed at the SLS 2.0. Everything but the detector system is in an ultrahigh vacuum (UHV) environment. The source of the SR light is a bending magnet. In case of a breach in a beamline's vacuum, machine safety requires all beamlines to be equipped with vacuum safety valves to protect the machine. Since FZPs are chromatic, a monochromator is installed prior to the first FZP. X-ray SR light is selected by the Si(111) channel-cut crystal monochromator set to a specific Bragg angle. With the configuration of one FZP or TXM, imaging can be realized at two different photon energies, for which the geometries match.

To lower the thermal load on the monochromator crystal, upstream apertures with fixed widths (2×2 mm) and an aluminum foil (200 μm thick) are inserted into the beam. The channel-cut Si(111) crystal of the monochromator is mounted on a copper block with indium foil between the crystal and copper surfaces for improved thermal contact. The copper block is water-cooled using the facility cooling water supply. The Bragg angle of the monochromator is set using a swivel stage, and it vertically displaces the beam.

The detector system consists of a 100 μm thick Ce:YAG scintillator (Crytur), images with a 5X Plan Apo infinity-corrected objective (Mitutoyo), and a CMOS camera (Basler acA4024-8gm).

The FZP alignment procedure is simple. First, the center position of the x-ray beam reflected by the Si crystal (corresponding to the position of the optical axis) is measured with the imaging system without FZP imaging. After that, the OZP is inserted and adjusted to the optical axis. Once the OZP has been aligned on the optical path, a clear radiography image of the OZP can be seen on the detector.

Since the vacuum chambers and imaging system are mounted at the design distances, once the OZP has been inserted, the monochromator Bragg angle is moved until the beam is focused onto the Ce:YAG scintillator. The single OZP is focused at 5.67° or 20 keV, which matches the FZP focal length for those distances. A tungsten circular block called the central stop (CS) is mounted on the OZP holder to block the direct beam and the higher harmonics of the monochromator that can blur the image. In the shadow of the CS, a clean image of the beam is obtained.

To ease the alignment of the MZP with respect to the OZP, markers visible in the radiography image were fabricated around the MZP membrane substrate (Fig. 2). To align the MZP, it was first inserted to overlap the OZP image, then the monochromator was moved to lower photon energy until the magnified beam spot was clearly focused on the Ce:YAG.

For the single OZP setup, the electron beam source is (de)magnified by 0.445. With the TXM setup, an image of the electron beam source at the bending magnet is magnified by a factor of 4.96 on the image plane.

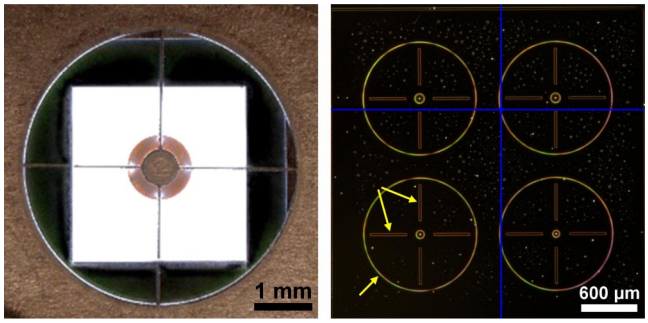


FIG. 2. (Left) OZP mounted with the central stop such that the CS faces the beam first. The CS was aligned to the zone plate under a laboratory microscope. (Right) Four MZPs on a single frame as imaged under the microscope. The yellow arrows indicate the alignment markers around the MZP.

Before installation, the FZP holder's tilt angles were aligned with respect to the optical path in the mechanical precision lab (Paul Scherrer Institute [PSI]) to be less than 50 μrad.

B. Fresnel zone plates

The FZPs were fabricated at PSI using electron beam lithography and gold electrodeposition [10]. The specifications of the FZP are summarized in Table II. The zones are made of gold on a silicon nitride membrane substrate

TABLE II. Specifications of the OZP as a single x-ray lens and as part of the TXM, the MZP, and the imaging system.

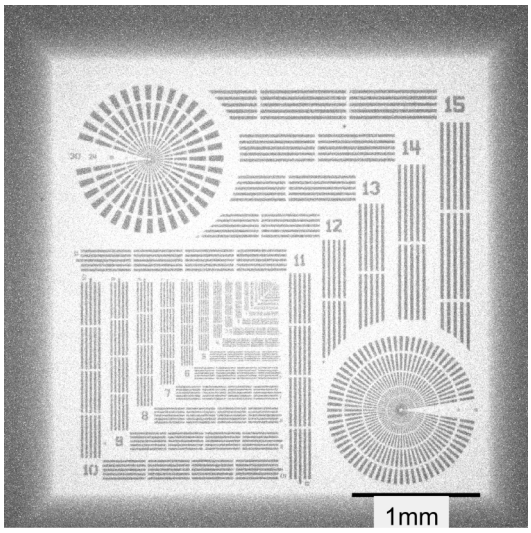
OZP parameters	11.8 keV/20 keV
Diameter (mm)	1.2
Zone width (nm)	120
Number of zones	2499
Focal length (mm)	1370.5/2322.9
OZP to focus (mm)	1677.0/3338.4
OZP magnification (M_{OZP})	0.223/0.445
Central stop diameter (mm)	0.6
MZP parameters	**11.8 keV**
Diameter (μm)	60
Zone width (nm)	120
Depth of focus (μm)	274.11
Number of zones	124
Focal length (mm)	68.53
MZP magnification (M_{MZP})	22.2
TXM parameters	
OZP focus to MZP distance (mm)	71.6
MZP to detector distance (mm)	1589.8
X-ray microscope length (mm)	3338.4
Total magnification (M)	4.96
Detector system parameters	
Visible magnification	5×
Numerical aperture (NA)	0.14
Camera pixel size (μm)	2.74

supported by a frame made of silicon. The parameters of the OZP as used alone (at 20 keV, 0.62 Å) and the TXM (at 11.8 keV, 1.06 Å) are summarized in Table II.

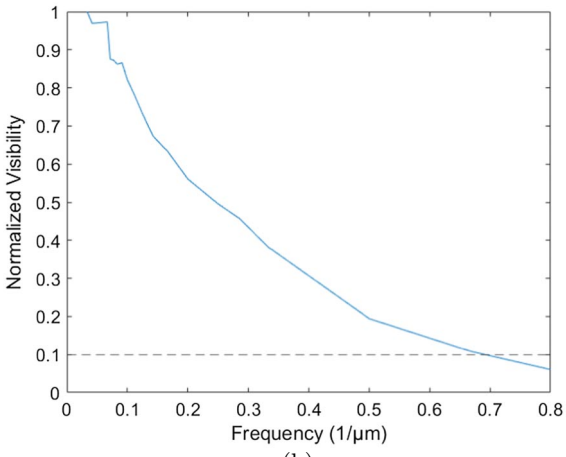
C. Spatial resolution

To measure a small beam profile, the spatial resolution of the beam size monitor must be significantly smaller than the beam size. The final spatial resolution of the monitor is determined by the diffraction limit of x-ray SR light (σ_{SR}), the Rayleigh resolution of the FZP (σ_{FZP}) [5], and the point spread function (PSF) (σ_{PSF}) of the imaging system.

Rayleigh diffraction (first-order diffraction on the focal plane) of the FZPs determines the limit of the measurable beam size with the FZP, which is given by $\sigma_{FZP} = 1.22 \cdot \Delta r_N$, where Δr_N is the outermost zone width. For both OZP and MZP, the outermost zone widths are 120 nm. The spatial resolution for a point-source image, determined by OZP alone, is limited by the demagnification of the OZP, $\sigma_{OZP} = \sigma_{FZP}/M_{OZP} = 0.33$ μm, where M_{OZP} is the magnification of the OZP. The resolution determined by the TXM is $\sigma_{TXM} = \sigma_{FZP} \cdot M_{MZP}/M = 0.65$ μm, where M is the total magnification of the TXM.



(a)



(b)

FIG. 3. (a) Image of the resolution target used to measure the detector system's PSF; (b) the plot shows the visibility measured from the target with respect to the line frequency, from which MTF10 (frequency corresponding to visibility at 0.1 as shown by the dashed horizontal line) is determined.

TABLE III. Resolutions of the OZP and the TXM setups.

Resolution contributions	
σ_{OZP} (μm):	0.33
σ_{TXM} (μm):	0.65
σ_{PSF} (μm):	1.5
Total spatial resolution	
$\sigma_{OZP,tot}$ (μm):	3.4
$\sigma_{TXM,tot}$ (μm):	0.72

If a single FZP system could be built without space restrictions, it would be possible to get closer to the diffraction limit of the FZPs, which is 146 nm for an FZP with an outermost zone width of 120 nm.

The lower limit to the measurable beam size with the OZP is dictated by the detector system, making accurate knowledge of its PSF crucial. The PSF is a convolution of several components: the NA of the microscope objective, the scintillator thickness, and the camera pixel size. We measured the modulation transfer function (MTF) [11] of the detection system using a resolution target (XRnanotech, Fig. 3). The contribution of the detector system (MTF10) was measured to be 1.5 μm at the image plane. For the TXM, where the source is magnified by a factor of 4.96 on the scintillator, the PSF is not dominant.

The total spatial resolution is estimated from the square root of the sum of the squares of these resolutions. The expected total spatial resolution of the OZP setup results in about 3.4 μm rms at the source plane due to demagnification. The total spatial resolution of the TXM is 0.72 μm rms at the source plane. These have been summarized in Table III. From here on, all measurements quoted are the deconvolution of these resolutions.

III. BEAM SIZE MONITOR CHARACTERIZATION

The vertical emittance in a storage ring is determined by quantum excitation, radiation damping (see, e.g., Ref. [12]), and coupling of the transverse optical functions. Since the contribution of quantum excitation is intrinsic but typically negligible, the vertical emittance is dominated by the coupling.

In light-source storage rings, especially for the lower-energy machines, the beam lifetime is primarily limited by Touschek scattering, and electrons are continuously lost over time. It is therefore important to increase the vertical emittance in a controlled manner in order to reduce the

electron density of the beam when necessary. For this purpose, the SLS 2.0 ring is equipped with skew quadrupoles to regulate transverse coupling. These skew quadrupoles are integrated into the octupole magnets as additional coil windings. A total of 264 octupole magnets are installed, providing a large number of accompanying skew quadrupoles.

Initially, transverse coupling depends on machine construction errors, primarily magnet misalignments. As preparation for controlling vertical emittance, a set of skew-quadrupole settings is determined to compensate for these errors. This step minimizes the vertical emittance to a baseline from which the linear coupling can be easily regulated.

Subsequently, either a precomputed or an experimentally determined skew-quadrupole setting is added to increase the vertical emittance. Using the available 264 skew quadrupoles, transverse coupling can be suppressed in the straight sections—where small-gap undulators are installed—while finite coupling and finite vertical dispersion are introduced along the arcs. The additional setting is scalable, allowing convenient adjustment of the vertical emittance and, consequently, the vertical beam size. This additional setting is referred to as the *vertical knob* hereafter. During user operation, it is configured to yield a vertical emittance close to the design value of 10 pm rad, which corresponds to a vertical knob of 100%. The vertical beam size is linearly proportional to the vertical knob setting.

Using OZP alone, source sizes have been measured at exposure times down to 1 ms for the operation beam current of 400 mA. However, for sufficient signal-to-noise ratio, the exposure time is set to 20 ms. The TXM requires a longer integration time due to the decrease in efficiency using the OZP and MZP in tandem. The camera integration time is of the order of hundreds of milliseconds.

During regular machine operation, the single OZP is used to monitor the beam size. The MZP is only inserted into the beam path for beam studies where small beam sizes are expected (Fig. 4).

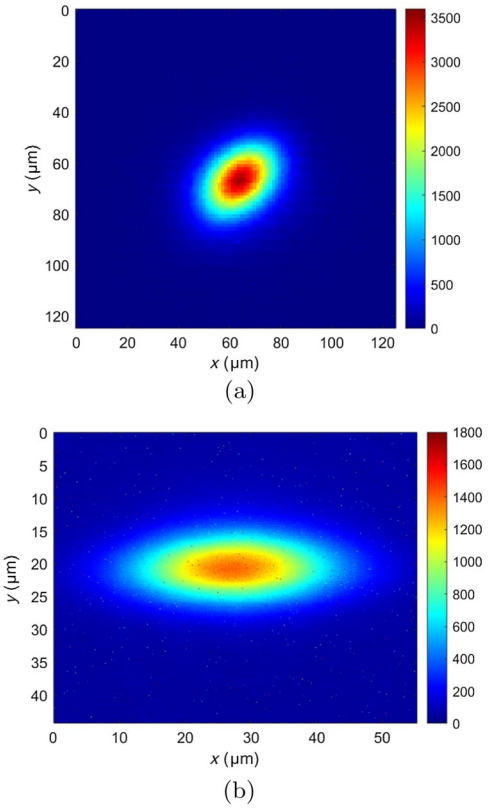


FIG. 4. (a) OZP is used to profile the beam for standard operation settings. The tilt in the beam is due to coupling and comparable dispersion in both horizontal and vertical planes. The beam size is $\sigma = 10.5 \times 9.7$ μm rms at 100 mA; (b) TXM is used to profile the beam at low vertical emittances ($\sigma = 3.8 \times 10.8$ μm rms at 100 mA).

A. Early commissioining observations

During the early stages of SLS 2.0 machine commissioning, the stored beam current was ramped up slowly over time to protect the radio frequency (rf) systems [13]. This cautious approach was particularly important when collective effects, which can potentially lead to damage to the rf system, were not yet studied.

Initially, the observed beam sizes were many times larger than the design values [8,14]. This was primarily attributed to suboptimal vacuum conditions in the machine. Residual gas molecules in the vacuum chamber cause beam scattering, which leads to emittance growth and consequently enlarged beam sizes. This effect is especially pronounced in SLS 2.0, where even localized pressure bumps can result in measurable emittance degradation. The SLS 2.0 vacuum system employs nonevaporable getter coated chambers to achieve the required UHV conditions [15–17].

In order to reach the required UHV conditions, the vacuum chamber must be *scrubbed* by the stored beam. During this process, synchrotron radiation photons and secondary electrons stimulate the desorption of gas molecules from the inner surfaces of the vacuum chamber, which are subsequently removed by the pumping system [16,17]. This progressively reduces the dynamic pressure in the ring. A particular challenge for SLS 2.0 is the use of a large number of small-aperture vacuum chambers required by the compact lattice [8,16], which increases the sensitivity to pressure spikes and makes thorough vacuum scrubbing essential. Over months of operation, with ever-increasing beam current (or beam dose given in ampere-hours), the vacuum conditioning improved significantly [15], leading to a measurable reduction in the observed beam size as the machine approached its design emittance. This can be seen in Fig. 5, where the vertical beam size decreases from 22.6 μm at 370 mA and a beam dose of 142 Ah to 15 μm at 350 mA for a beam dose of 258 Ah.

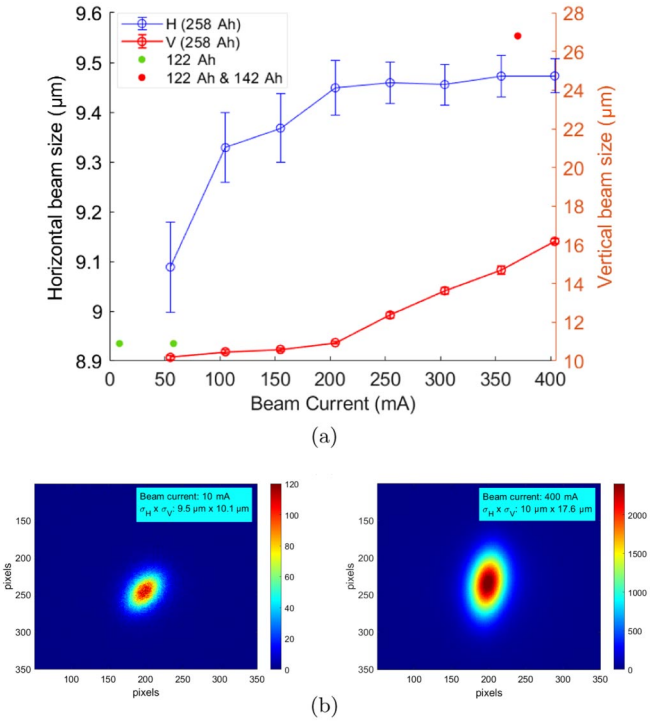


FIG. 5. (a) Changes in beam size over time and with increasing beam current, as measured with the OZP setup. The red and green dots show that, over time, beam scrubbing leads to a decrease in the measured beam size and suppressed ion instabilities. Primarily due to gas scattering, the beam size increases with beam current. (b) Representative images of the beam profiles at 10 and 400 mA. At low currents, beam scattering is not a dominant effect, but at high currents, the effect of suboptimal vacuum shows in the beam blow-up.

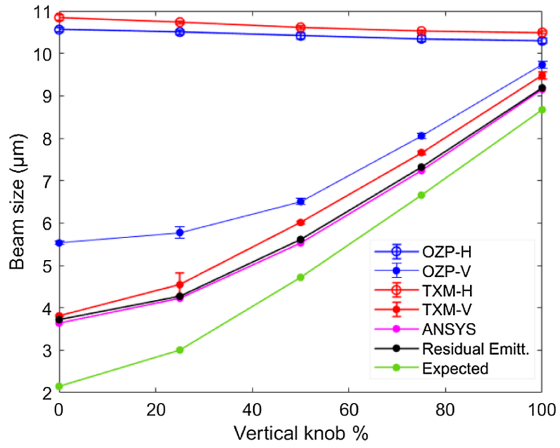


FIG. 6. Beam size as measured with the OZP (blue) and with the TXM (red) for various vertical knob settings. The modeled and measured vertical beam size is shown with dots, and the measured horizontal is shown with circles. The ideally expected vertical beam sizes for these knob settings are shown in green. In black are the computed beam sizes for a residual emittance of 3 pm rad, and the magenta dots show the simulated beam size for a monochromator with a deformed surface.

The beam size increase with beam current becomes less significant when vacuum is improved.

B. Vertical beam size variation

To determine the limits of the TXM, the vertical knob was adjusted to reduce the vertical beam size. This measurement was done at a beam current of 100 mA. Due to the decrease in photon flux with the MZP, the exposure time of the camera for TXM setup is 800 ms. The OZP data were acquired at 10 ms exposure time. The S/N for TXM is 14 times smaller than the S/N of the OZP. For this reason, 50 images were averaged, and the Gaussian fitting was done on the projection of the image in each dimension. Figure 6 shows the beam sizes measured by the OZP and the TXM. As can be seen, the OZP measurements do not resolve the small beams accurately. The OZP demagnifies the beam on the imaging plane where the PSF dominates. The TXM setup ($M = 4.96$) is designed for resolving small beams where the OZP is limited. With the TXM, the smallest beam size measured with a flat lattice (vertical knob removed) is 3.8 μm. This translates to 1.7 μm on the image plane with the OZP, which is close to the PSF (1.5 μm).

For vertical knob settings $> 50\%$, the differences between the OZP and TXM beam sizes are < 0.2 μm. Although these beam sizes are larger than the PSF and the sampling is sufficient, these measurements demonstrate that TXM is required to accurately measure the beam size and verify the OZP measurements. The difference in the horizontal beam sizes measured with the OZP and the TXM is within 2%–3% across the range of the applied vertical knob. However, the expected horizontal beam size change due to coupling is below 0.1%. This may indicate that the vertical knob could also change the beta function and dispersion in the horizontal plane. This is currently under investigation.

One possible candidate for the difference between the expected and measured beam sizes is the mechanical deformation of the first surface of the channel-cut monochromator. The monochromator crystal was installed into the vacuum chamber at a temperature below that of the cooling water supply (25°C). As the crystal warms up, the resulting thermal expansion deforms the reflecting surface. There could also be additional deformations due to absorbed beam power. For this study, ANSYS was used to model the surface deformation for: (1) the expected beam power on the first surface; (2) a crystal that was mounted at 20°C while the cooling water is at 25°C (as is at SLS 2.0). The output from the ANSYS model (Fig. 7) was used to simulate the effect of the surface deformation on the beam size measured with the TXM setup, using the SHADOW API in OASYS [18]. The resulting data are shown in magenta in Fig. 6.

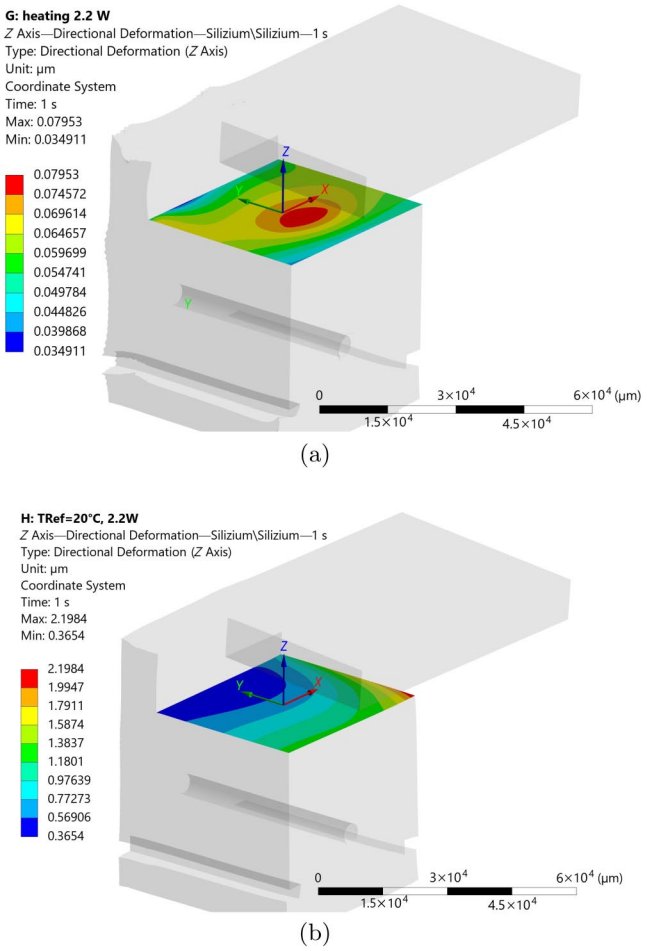


FIG. 7. ANSYS modeling of surface distortion of the channel-cut monochromator crystal due to (a) input beam power of 2.2 W; (b) deformation by the difference in crystal mounting temperature and the cooling water supply. The latter is the dominant effect.

The discrepancy observed with the OZP at 20 keV can be attributed to the monochromator crystal deformation. At 20 keV, the smaller Bragg angle results in a more elongated beam footprint on the crystal. The beam samples more of the deformed surface and is therefore exposed to more slope errors. This accounts for the larger deviation observed with the OZP relative to the TXM case.

Another plausible explanation for the discrepancy is residual vertical emittance after coupling correction. The coupling correction was performed a few months before the data of Fig. 6 was acquired, and due to machine drifts over time, the residual vertical emittance might be sizeable. Such drifts indeed necessitate constant beam monitoring during machine operation. Additionally, the coupling control in SLS2.0 is not yet fully developed. To approximately evaluate possible residual vertical emittance at the time of data acquisition, we computed the vertical beam sizes by adding the contributions of various residual vertical emittances to the expected ones and found that a residual emittance of 3 pm rad corresponds to the aforementioned effect of crystal deformation. This has been depicted for the TXM setup in the plot in Fig. 6 in black. The discrepancy is likely due to a combination of these two factors, namely, monochromator deformation and residual emittance.

C. Vibrations

Stability of the monitor is crucial for the measurement of small beams, as any vibrations in the setup may affect the outcome. Possible sources for vibrations in the setup are cooling water distribution to beamline components such as the monochromator, servo motors on which the detector system sits, and membrane vacuum pumps.

We measured vibrations by running the camera at 236 frames per second and using the OZP alone to measure the variation in the position of the center-of-mass of the beam in both horizontal and vertical directions. The power spectral density of this data reveals that the total contributions from the setup (V: 0.19 μm, H: 0.21 μm rms) are negligible to the overall measured beam sizes.

IV. CONCLUSIONS

In-vacuum x-ray Fresnel zone plates are used in a single (OZP) and dual (TXM) configuration at the SLS 2.0 to obtain continuous electron beam size measurements from a bending-magnet source. A longer setup would simplify measurements with a single FZP but is not possible within the current length constraints.

Although a TXM setup has been built, during normal operations, the single OZP configuration is sufficient to accurately monitor beam sizes down to about 9 μm rms with a minimum exposure time of 1 ms.

By varying the vertical beam sizes, it was possible to compare the performance of the OZP and the TXM setups. For the current setup, it can be concluded that for beam sizes below 9 μm, the TXM should be used instead. This is not a limitation due to the technique but potentially due to the monochromator crystal's surface deformation.

Several improvements are planned to enhance system performance. To reduce surface deformation, the monochromator crystal will be reinstalled at the same temperature as the cooling water. Further machine studies will be required to validate the accuracy of the measurements.

Since the spatial resolution is dominated by the resolution of the detector setup, a microscope objective with a larger magnification will be installed. To improve the S/N of the TXM setup, the microscope objective will also have a larger numerical aperture. The larger NA will make it possible to collect more light and reduce the exposure time of the camera. The camera is currently not synchronized to beam injections. It is planned to synchronize the camera to beam injections for machine studies on transverse beam profile evolution, beam stability, and injection efficiency.

The commissioning of SLS 2.0 is inherently an iterative process, whereby the diagnostics drive the optimization of the storage ring, and the progressively improving beam quality and stability further enables the refinement of the diagnostic systems.

ACKNOWLEDGMENTS

The authors would like to thank all the technical specialist groups, A. Fazan, A. Foskolos, A. Streun, N. Samadi, X. Shi, J. Kallestrup, and F. Armborst for their support from the beginning of the SLS 2.0 project and throughout commissioning. The nanolithography work was carried out in the PICO clean room facility (PSI).

DATA AVAILABILITY

There are no publicly available research data or software supporting this manuscript. Requests for further information or data should be sent to the authors.

[1] C. Thomas, G. Rehm, I. Martin, and R. Bartolini, X-ray pinhole camera resolution and emittance measurement, Phys. Rev. ST Accel. Beams **13**, 022805 (2010).

[2] C. L. Li, Y. H. Xu, M. J. Boland, T. Mitsuhashi, W. J. Zhang, M. Grinberg, and J. Corbett, Double-slit interferometer measurements at SPEAR3, in *Proc. IPAC'16* (Busan, Korea, 2016), pp. 368–370, 10.18429/JACoW-IPAC2016-MOPMR054.

[3] N. Samadi, X. Shi, L. Dallin, and D. Chapman, Source size measurement options for low-emittance light sources, Phys. Rev. Accel. Beams **23**, 024801 (2020).

[4] K. Iida, N. Nakamura, H. Sakai, K. Shinoe, H. Takaki, M. Fujisawa, H. Hayano, M. Nomura, Y. Kamiya, T. Koseki, Y. Amemiya, N. Aoki, and K. Nakayama, Measurement of an electron-beam size with a beam profile monitor using Fresnel zone plates, Nucl. Instrum. Methods Phys. Res., Sect. A **506**, 41 (2003).

[5] H. Sakai, M. Fujisawa, K. Iida, I. Ito, H. Kudo, N. Nakamura, K. Shinoe, T. Tanaka, H. Hayano, M. Kuriki, and T. Muto, Improvement of Fresnel zone plate beam-profile monitor and application to ultralow emittance beam profile measurements, Phys. Rev. ST Accel. Beams **10**, 042801 (2007).

[6] S. Takano, M. Masaki, and H. Ohkuma, X-ray imaging of a small electron beam in a low-emittance synchrotron light source, Nucl. Instrum. Methods Phys. Res., Sect. A **556**, 357 (2006).

[7] C. Ozkan Loch, M. Gregorio, R. Ischebeck, N. Samadi, and J. Vila-Comamala, Beam size measurement developments at SLS, in *JACoW IPAC2023*, Venice, Italy (JaCow, 2023), pp. 4814–4816, 10.18429/JACoW-IPAC2023-THPL148.

[8] H. Braun *et al.*, SLS 2.0 storage ring technical design report, PSI Bericht 21-02, Paul Scherrer Institute, 2021.

[9] A. Streun, M. Aiba, M. Böge, C. Calzolaio, M. Ehrlichman, M. Negrazus, B. Riemann, and V. Vrankovic, Swiss Light Source upgrade lattice design, Phys. Rev. Accel. Beams **26**, 091601 (2023).

[10] S. Gorelick, V. A. Guzenko, J. Vila-Comamala, and C. David, Direct e-beam writing of dense and high aspect ratio nanostructures in thick layers of PMMA for electroplating, Nanotechnology **21**, 295303 (2010).

[11] S. N. Ahmed, *7—Position-Sensitive Detection and Imaging, Physics and Engineering of Radiation Detection*, 2nd ed. (Elsevier, New York, 2015), pp. 435–475, ISBN 9780128013632, 10.1016/B978-0-12-801363-2.00007-3.

[12] T. O. Raubenheimer, The Generation and acceleration of low emittance flat beams for future linear colliders, SLAC Report 387, p. 19, Stanford Linear Accelerator Center, 1991.

[13] R. Ganter *et al.*, SLS 2.0 Storage ring upgrade overview, in *Proc. IPAC* (Taipei, Taiwan, 2025), pp. 79–82, 10.18429/JACoW-IPAC2025-MOPB005.

[14] A. Streun *et al.*, SLS-2–The upgrade of the Swiss Light Source, J. Synchrotron Rad. **25**, 631 (2018).

[15] N. Kirchgeorg *et al.*, A new NEG coating setup with travelling thin solenoids for the SLS 2.0 complex vacuum chambers, J. Phys.: Conf. Ser. **2687**, 082028 (2024).

[16] R. Ganter, P. Braschoss, H.-H. Braun, J. Buchmann, A. Citterio, M. Dehler, N. Gaiffi, N. Kirchgeorg, M. Magjar, C. Rosenberg, D. Stephan, L. Schulz, R. Sieber, X. Wang, and A. Zandonella, Vacuum chambers for Swiss Light Source arcs, Phys. Rev. Accel. Beams **27**, 053201 (2024).

[17] R. Ganter, P. Braschoss, J. Buchmann, A. Citterio, M. Dehler, N. Gaiffi, N. Kirchgeorg, M. Magjar, C. Rosenberg, D. Stephan, L. Schulz, R. Sieber, and X. Wang, SLS 2.0 vacuum components design, in *Proc. IPAC 2023* (Venice, Italy, 2023), pp. 4301–4304, 10.18429/JACoW-IPAC2023-THPA147.

[18] L. Rebuffi, M. Sanchez del Rio, K. Sawhney, and O. Chubar, OASYS (OrAnge SYnchrotron Suite): An open-source graphical environment for x-ray virtual experiments, in *Proc. SPIE 10388, Advances in Computational Methods for X-Ray Optics IV, San Diego, California, USA* (2017), p. 103880S, 10.1117/12.2274263.